The Influence of Floodplain Channel Connectivity on Flood Hydrodynamics

Scott Robert David[1], Jonathan A. Czuba[2], Douglas Arthur Edmonds[3], and Adam Scott Ward[3]

[1]University of Massachusetts Amherst
[2]Virginia Tech
[3]Indiana University Bloomington

November 26, 2022

Abstract

High-resolution topographic data reveal that meandering river floodplains can contain complex floodplain-channel networks. However, the influence of this topography on flood initiation and progression is unknown. In this study, we investigate how floodplain-channel networks influence flooding processes in low-gradient river systems. To accomplish this, we conducted a series of numerical modeling experiments using a two-dimensional (2-D) model built in Hydrologic Engineering Center's River Analysis System (HEC-RAS). First, we simulated floods using 2-D HEC-RAS on the East Fork White River near Seymour, IN, USA, including the current, dense network of floodplain channels. Next, we simulated synthetic versions of this river system where we varied the connectivity among floodplain channels, and also between the floodplain channels and river channel. We found distinct differences in flooding patterns and flood hydraulics among model simulations. Numerical modeling experiments showed that increasing floodplain channel connectivity caused increased spatial variability of wet and dry surfaces across the floodplain, increased residence time of water on the floodplain, and increased floodwave attenuation. Results from this study indicate that topographic connectivity on the floodplain challenges the classic notions of flooding initiation, and potentially increases a floodplains ability to store matter.

The Influence of Floodplain Channel Connectivity on Flood Hydrodynamics

Scott R. David[1,2], Jonathan A. Czuba[3], Douglas A. Edmonds[2], and Adam S. Ward[4]

[1]Department of Geosciences, University of Massachusetts, Amherst, Massachusetts, USA

[2]Department of Earth and Atmospheric Sciences, Indiana University, Bloomington, Indiana, USA

[3]Department of Biological Systems Engineering and The Global Change Center, Virginia Tech, Blacksburg, Virginia, USA

[4]School of Public and Environmental Affairs, Indiana University, Bloomington, Indiana, USA

Corresponding author: Scott David (sdavid@umass.edu)

Key Points:

- Well-connected floodplain channels promote increased spatial variability in flooding and changes how floodplains fill with water.
- Floodplain channel connectivity influences flood hydraulics and floodwave propagation at low flooding discharges.
- Intermediate connectivity among floodplain channels and the river channel maximizes lateral exchange and residence time of floodwaters.

Abstract

High-resolution topographic data reveal that meandering river floodplains can contain complex floodplain-channel networks. However, the influence of this topography on flood initiation and progression is unknown. In this study, we investigate how floodplain-channel networks influence flooding processes in low-gradient river systems. To accomplish this, we conducted a series of numerical modeling experiments using a two-dimensional (2-D) model built in Hydrologic Engineering Center's River Analysis System (HEC-RAS). First, we simulated floods using 2-D HEC-RAS on the East Fork White River near Seymour, IN, USA, including the current, dense network of floodplain channels. Next, we simulated synthetic versions of this river system where we varied the connectivity among floodplain channels, and also between the floodplain channels and river channel. We found distinct differences in flooding patterns and flood hydraulics among model simulations. Numerical modeling experiments showed that increasing floodplain channel connectivity caused increased spatial variability of wet and dry surfaces across the floodplain, increased residence time of water on the floodplain, and increased floodwave attenuation. Results from this study indicate that topographic connectivity on the floodplain challenges the classic notions of flooding initiation, and potentially increases a floodplains ability to store matter.

1.0 Introduction

River floodplains are a key human habitat (Di Baldassarre et al., 2013) that provide rich, fertile soils for agriculture, and are among the most productive ecosystems on Earth (Tockner & Stanford, 2002). These ecosystems depend on surface-water connectivity between rivers and floodplains, which ultimately controls bioproductivity, biodiversity, and biogeochemical cycling in floodplains (Costanza et al., 1997; Malard et al., 2002). Surface-water connectivity refers to the exchange of water, and particulate matter between the river and floodplain (Junk et al., 1989; Mitsch & Gosselink, 2000; Tockner & Stanford, 2002; Walling, 1999). At timescales shorter than appreciable surface morphological change, surface-water connectivity is the result of a time-variable hydrograph that drives surface-water (Covino, 2017; Junk et al., 1989; Ward & Stanford, 1995) and hyporheic exchange (Boulton, 2007; Roley et al., 2012; Stanford & Ward, 1993). The geomorphic surface, which is assumed to be static on timescales of individual events, controls the transfer of water, energy, and material between the river and floodplain, and can change in both time and space through natural and anthropogenic processes (Bracken & Croke, 2007; Poeppl et al., 2012) . While most studies have focused on how a fluctuating hydrograph influences surface-water connectivity (e.g., Wohl et al., 2019), we flip the perspective and focus on how different floodplain geomorphic surfaces influence surface-water connectivity for a given hydrologic condition. This perspective is important because it will help us understand the important geomorphic attributes that drive surface-water connectivity (Wohl et al., 2019).

Floodplain geomorphic surfaces have many kinds of topographic features that can be connected and linked together (commonly called “structural connectivity”; Wainwright et al., 2011; Wohl et al., 2019). We define here the concept of “topographic connectivity” as one type of structural connectivity that specifically refers to what aspect of the structure is controlling connectivity. One important way floodplains become topographically connected is through formation of channels on the floodplain surface that transport water and sediment and connect otherwise distant parts of the floodplain with the main channel (Czuba et al., 2019; Mertes et al., 1996; Rowland et al., 2009). These floodplain channels are more than just the remnants of the main channel from cutoffs or avulsions; instead they can be an integrated network of channels on the floodplain surface, similar to a drainage network (David et al., 2017; Fagan & Nanson, 2004; Kupfer et al., 2015; Rak et al., 2016; Thayer & Ashmore, 2016; Trigg et al., 2012).

These networks form through headcutting (David et al., 2019) and create channels with morphologies and cross-sectional areas different from the main channel (David et al., 2017; Fagan & Nanson, 2004; Trigg et al., 2012). Despite the increasing awareness of floodplain-channel networks, only a few studies have explored their influence on floodplain processes and surface-water connectivity (Czuba et al., 2019; Trigg et al., 2012).

Floodplain networks create a distinct scale of topographic connectivity that controls when and where flooding begins and which paths floodwaters will take (Czuba et al., 2019). In fact, these floodplain-channel networks allow water to enter the floodplain from the main channel well before all banks are overtopped. This phenomenon has been observed in floodplains of the Amazon River in Brazil (Rudorff et al., 2014; Trigg et al., 2012), Congaree River in South Carolina (Kupfer et al., 2015), Medway River in southern Ontario (Thayer & Ashmore, 2016), West Fork White River, Indiana, USA (David et al., 2017), and the East Fork White River, Indiana, USA (Czuba et al., 2019). In a particularly compelling case, Czuba et al. (2019) conducted a study along the East Fork White River, Indiana, USA and showed that floodplain channels cause flooding at a 19-day recurrence interval (RI), even though banks were not fully inundated until a 9-month RI.

The overarching goal of this study is to test how the topographic connectivity of floodplain-channel networks—both within the network itself and between the network and main channel—affects flooding patterns. Specifically, we address three questions:

(1) How does the topographic connectivity between the floodplain and main channel influence spatial patterns of flooding and flooding extent? (2) To what degree does topographic connectivity within the floodplain-channel network influence hydraulics within the floodplain (e.g., depth, velocity)? and (3) How do river-to-floodplain and within-floodplain topographic connectivity influence surface-water residence time and lateral exchange between the river channel and floodplain? To address these questions, we extend the calibrated model from Czuba et al. (2019) of the East Fork White River near Seymour, IN, USA to account for fully unsteady flow. We conduct 2-D surface-water flow modeling in Hydrologic Engineering Center's River Analysis System (HEC-RAS) exploring flooding processes as a function of various degrees of topographic connectivity between the floodplain and river channel and the topographic connectivity among floodplain channels.

2.0 Study Site Description

Our study area is located along the East Fork White River between Columbus and Brownstown, IN, USA (Figure 1). We chose this location because it includes a long continuous floodplain containing floodplain channels (Figure 1) and has a high floodplain channel density (~7 floodplain channels per cross-section) making the East Fork White River an ideal setting to study the influence of topographic connectivity on flooding processes. Additionally, this reach contains a USGS gage (gage number 03365500) in the middle of the study area, just downstream of a low-head dam near Seymour, IN (Figure 1). The upstream extent of our study area has a drainage area of about 5,120 km^2. The only major tributary that enters the study area is Sand Creek, which drains 681 km^2 of the White River drainage basin into the East Fork White River. The downstream extent of the study area drains about 6,160 km^2 of land. Land cover in the model area is 75% agriculture, 13% vegetated/forested, 8% urban development, and 4% water (Homer et al., 2015). In the study reach, the main river channel has an average width of 73 m, an average bank height (river channel bottom to top of bank) of 3.8 m, a bed slope of 3×10^{-4} m m^{-1}, a sinuosity of 1.7 (David et al., 2017), and an average river bend migration rate of 3.4 m yr^{-1} (Figure 1; Robinson, 2013). In the model domain the floodplain averages 2,700 m wide and has a slope of 5×10^{-4} m m^{-1}. The floodplain channels along this reach begin to convey water when the river reaches a discharge of 268 $m^3 s^{-1}$ (19-day RI; Czuba et al., 2019).

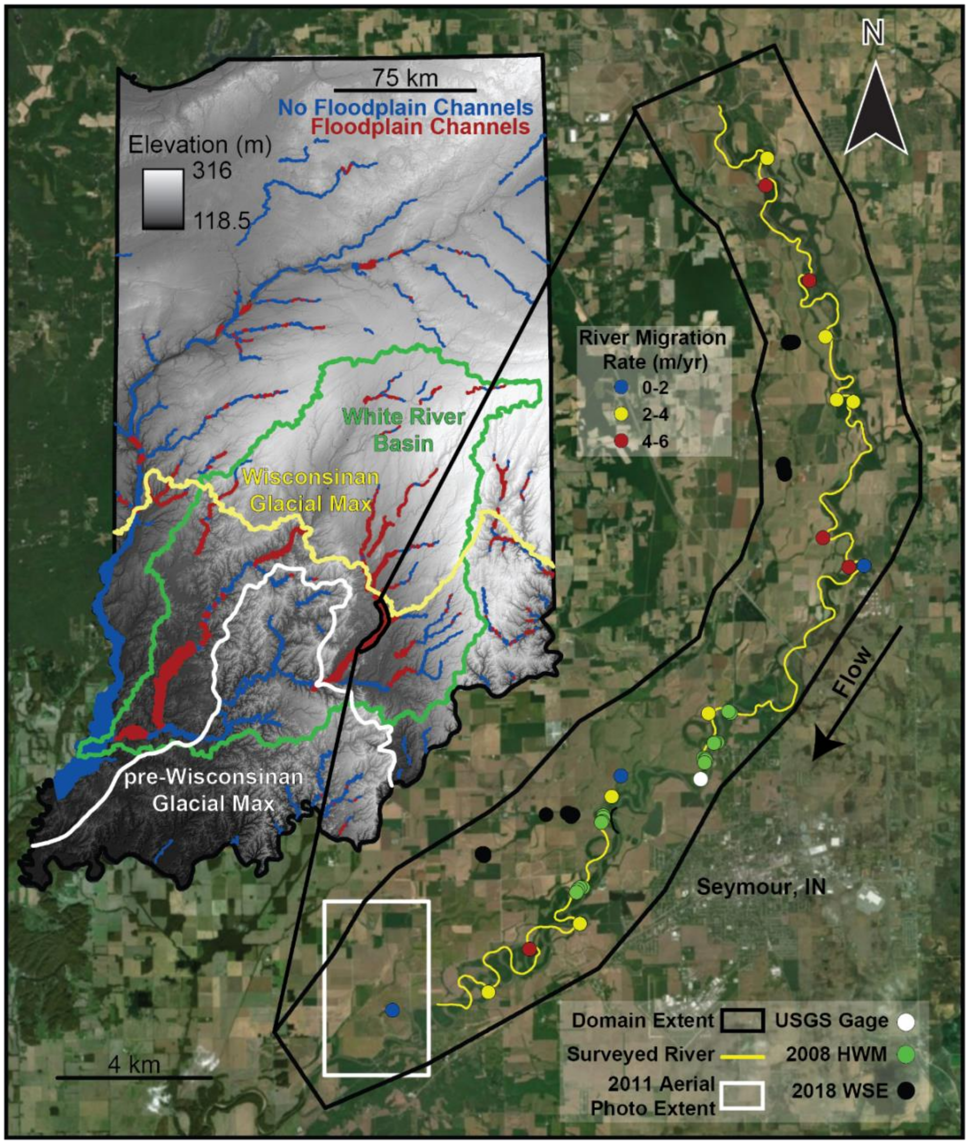

Figure 1. Study area of the East Fork White River. Imagery of the East Fork White River, where the study area is outlined in black. We show the locations of 2018 water surface elevations (WSE), 2008 high-water marks (HWM) collected by the USGS, and the USGS gage used for calibration and validation. Average river migration rates of specific bends are plotted as blue, yellow, and red dots with increasing migration rates, respectively (Robinson, 2013). The inset image shows the location of the White River drainage basin in Indiana (shown with a green line). The blue lines/polygons show floodplains without floodplain channels and the red lines/polygons show floodplains with floodplain channels (David et al., 2017). The maximum glacial extent of the

pre-Wisconsinan and Wisconsinan glaciations are shown with white and yellow lines, respectively.

3.0 Methods

3.1 Model Development

Czuba et al. (2019) developed and calibrated a model of the East Fork White River in 2D HEC-RAS and ran it under steady-state flow using the diffusive wave equations. In this study, we have recalibrated this model to run full unsteady flows using the Saint Venant equations. For a full description of the modeling methods see Czuba et al. (2019) or a stand-alone account of the full methods used here that partially overlaps with those of Czuba et al. (2019) in the supplementary information. In this section we note only the elements of the modeling effort that differ from Czuba et al. (2019). Topographic data used in modeling experiments were constructed from a 1.5 m DEM derived from airborne light detection and ranging (lidar) data and field surveyed bathymetric data. In addition to the existing topography, we also generated five synthetic floodplains based on the East Fork White River floodplain with various degrees of floodplain channel and river-floodplain topographic connectivity. The synthetic floodplain surfaces were generated by extracting the extent of the East Fork White River active floodplain at the 89-year flood of record (Czuba et al., 2019). We then removed all floodplain channels from the floodplain surface by applying a Gaussian filter (Eqn. 1) as:

$$G(x,y) = \frac{1}{\sqrt{2\pi\sigma^2}} e^{-\frac{x^2+y^2}{2\sigma^2}} \qquad \text{Eqn. 1}$$

where, x and y are spatial distances (m) and σ is the standard deviation of the Gaussian distribution (m). The calculation used σ = 6 m and iterated over the active floodplain 20 times, creating a preliminary smoothed floodplain. The presence of the floodplain channels caused artificially low elevations between floodplain channels during the Gaussian spatial averaging. To overcome this, we removed and interpolated all portions of the active floodplain more than 0.1 m below the preliminary smoothed surface. This eliminated most floodplain channels and the river channel. Additionally, we removed all major road features in the active floodplain domain to avoid any artificial increases in floodplain elevation. We applied the same Gaussian filter as before to the active floodplain with the floodplain channels, river channel, and roads removed, thus producing a smoothed version of the East Fork White River floodplain that maintains long wavelength topography. The river channel, roads, and terraces were then added back into the smoothed floodplain topography creating a floodplain with similar long wavelength topography and floodplain extent, but without floodplain channels (Figure 2).

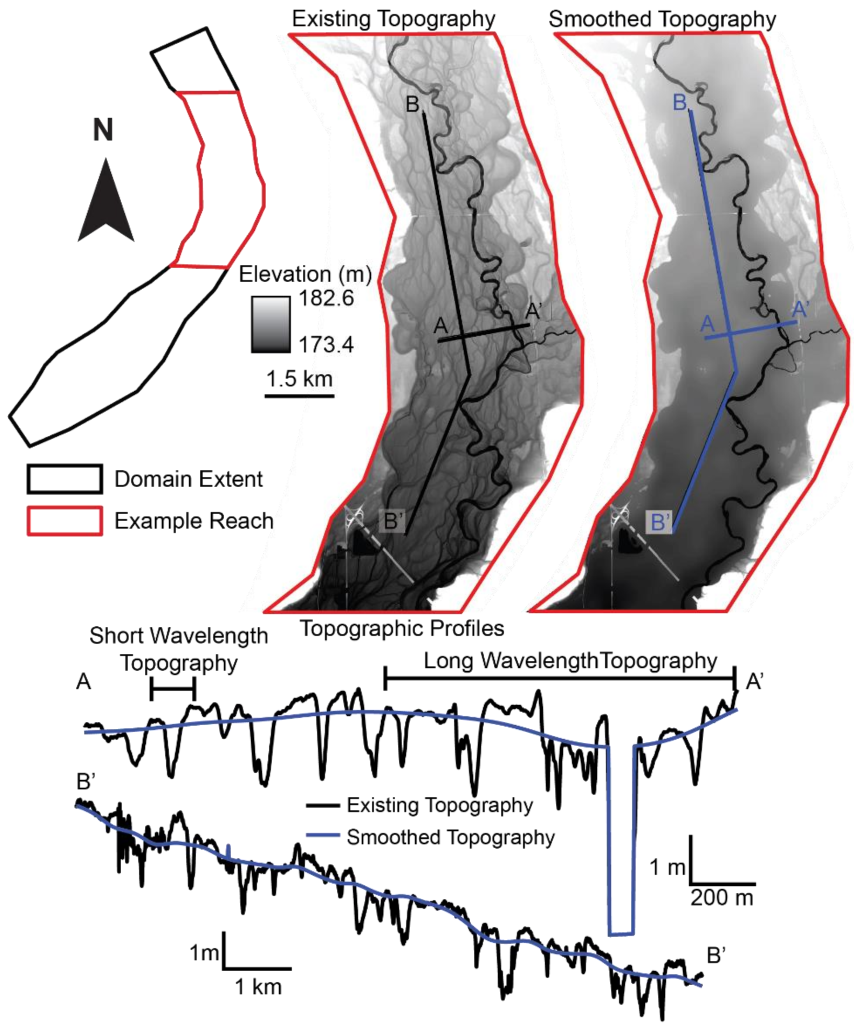

Figure 2. Smoothed floodplain topography. The left image shows the existing topography along the East Fork White River and the right image shows the smoothed topography after applying a Gaussian Filter. The topographic profiles illustrate how the Gaussian filter removed all floodplain channels, while maintaining long wavelength undulating topography.

We used the smoothed floodplain (Figure 3a) and existing floodplain (Figure 3f) to generate four additional synthetic floodplains with different topographic connectivity between the floodplain channels and the river channel. We envision different floodplain-channel network connectivity as being related to the degree of channelization. The present floodplain surface is channelized with a highly integrated floodplain-channel network, and the smooth floodplain surface is the least channelized. We create intermediately channelized floodplains by selectively preserving the deepest parts of the channel network. This creates a floodplain with channel segments that are not connected. To do this we detrend the natural floodplain with the smoothed floodplain, thereby creating a normalized DEM where negative values represent elevations lower than the smoothed floodplain. We then use two floodplain channel masks with threshold values of -0.23 m and -0.84 m and remove all channel cells above the thresholds. This creates two surfaces that isolate and preserve only the lowest-lying floodplain channel cells (threshold of -0.84 m) and both low-lying and mid-elevation floodplain channels (threshold of -0.23 m). The two channel masks were used to extract floodplain channels from the existing topography and add them back to the smoothed floodplain topography. The threshold of -0.84 m created a floodplain with weakly connected floodplain channels (Figure 3c), and the threshold of -0.23 m created a floodplain with better connected floodplain channels (Figure 3e).

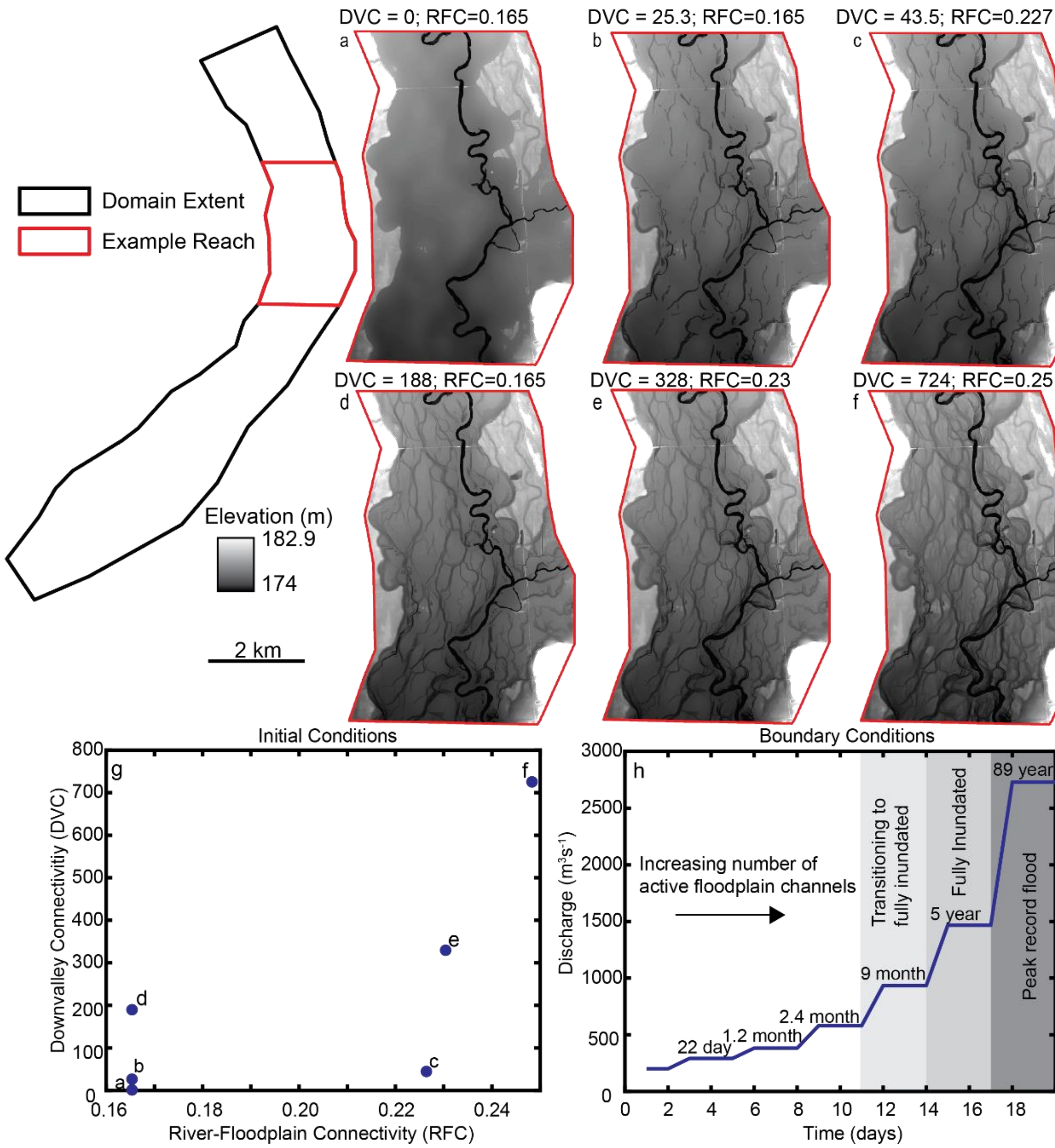

Figure 3. Initial and Boundary Conditions. a-f) Example reaches of the 6 initial conditions with varying down-valley floodplain channel connectivity (DVC) and river-floodplain channel connectivity (RFC). The illustration on the left shows the location of the example reaches, outlined in red, on our model domain, shown in black. g) Plot of parameter space for the calculated DVC and RFC values for the entire domain. The example reaches shown above are labeled (a-f) on the plot. h) Plot of total discharge used in our modeling. Each step is labeled with its respective RI. The shaded portions of the graph indicate the flooding extent for a given discharge reported by Czuba et al. (2019) used to guide our selection of discharges.

Additionally, we constructed two synthetic floodplains with the same floodplain-channel connectivity as described above, but we also changed the strength of connections between the floodplain channel and the main river (Figure 3b, d). To accomplish this, all floodplain channels were removed from the two floodplain channel masks within 60 m (approximately two times the average levee width) of the river channel. This effectively removes all natural breaks in the levees and banks created by channels or crevasses. We created one additional floodplain channel mask to delineate the floodplain channels on the existing floodplain using a threshold of -0.15 m. The mask was used for data analysis and quantifying initial conditions.

To quantitatively describe our six different floodplains initial conditions, we developed a metric to describe the connectivity within the floodplain-channel networks (hereafter down-valley connectivity, DVC). DVC was calculated as:

$$DVC = \frac{F_{CA}}{F_{TA}} \times F_I \qquad \text{Eqn. 2}$$

where, F_{CA} is the floodplain channel surface area (m^2), F_{TA} is the total floodplain area (m^2), and F_I is the number of floodplain segments surrounded by floodplain channels (an approximation to assess the number of floodplain channel connections). F_{CA} was calculated with the floodplain channel masks used to extract floodplain channels (described above). F_{TA} was measured based on the wetted extent of the 89-year flood (peak of record) from Czuba et al., (2019). Hence, larger DVC values indicate a greater number of well-connected floodplain channels across the floodplain.

Similarly, we describe the connectivity between the floodplain and main channel as river-floodplain connectivity (RFC). RFC was computed as the coefficient of variation (standard deviation/mean) of the bank height within 30 m (approximately average levee width) of the river channel (Figure 3g). Larger RFC values represent river banks with higher topographic variability, hence an enhanced connection of the river channel to floodplain channels.

3.2 Boundary Conditions

The upstream boundary conditions were specified along the East Fork White River and Sand Creek as a quasi-steady state discharge entering the domain (see Fig. S1 and supplemental methods). The downstream boundary condition was set to maintain normal depth exiting the domain. The quasi-steady state simulations held the discharge entering the domain constant until equilibrium was achieved throughout the entire domain before increasing the discharge (Figure 3h). Our model simulated six discharges ranging from 292 m^3s^{-1} to 2,730 m^3s^{-1} which spanned a range of floodplain inundation extents (Czuba et al., 2019; Figure 3h). The six simulated discharges and six initial conditions created a total of 36 simulations exploring steady state discharges.

In a second set of experiments, we relax the assumption of steady flow and explore flood wave propagation. For floodwave propagation the model setup was identical to those for the steady state simulations; however, we specified no discharge entering the domain along the sand creek boundary condition and specified a hydrograph at the upstream boundary for the East Fork White River. The input hydrographs were triangular shaped that had peak discharges of 292 m^3s^{-1}, 581 m^3s^{-1}, and 1467 m^3s^{-1}, respectively. The rising limb of the floodwave increased at a rate of 18.7 m^3s^{-1} per hour and the falling limb decreased at a rate of 8.2 m^3s^{-1} per hour. The rates for rising and falling floodwave limb is based on a 10-year average of all rising and falling limbs of floodwaves at the gage in Seymour, IN (USGS, 2018).

3.3 Calibration and Validation

We calibrated the model to the elevation-discharge rating curve developed for the USGS gage located near Seymour, IN (Figure 1). Model calibration was conducted by varying Manning's roughness coefficients for the open water (river channel) and agricultural land cover classes (Homer et al., 2015). Final roughness coefficients for the open water and agricultural land cover classes were 0.022 and 0.025 (Table S1), respectively. The final calibrated roughness coefficients in our study differs from those in Czuba et al. (2019) due to the use of the Saint Venant equations rather than the diffusive wave equations. Comparing our model simulations to the elevation-discharge rating curve (USGS, 2018), we obtained a root mean squared error (RMSE) of 0.16 m and a mean average error (MAE) of 0.15 m (Figure S2). Model performance is comparable to that reported by Czuba et al., (2019). For an extended discussion of model calibration and validation, see supplementary information.

3.4 Data Analysis

Initial model outputs from our 36 modeling experiments included water depth, depth averaged velocity magnitude, and 2-D (x and y directed) depth averaged velocity for each cell. We gridded the results at a 15-m resolution for all analysis. From the initial model outputs, we computed the magnitude of specific discharge (q, m^2 s^{-1}; Eqn. 3) and a 2-D specific discharge ($q_{x,y}$, m^2 s^{-1}; Eqn. 4) for each grid cell in all model simulations as:

$$q = \bar{v} * h \qquad \text{Eqn. 3}$$

and

$$q_{x,y} = \overline{v_{x,y}} * h \qquad \text{Eqn. 4}$$

where, $\bar{v}$ is the depth-averaged magnitude of velocity (m s^{-1}), h is water depth (m), and $\overline{v_{x,y}}$ is the 2-D depth-averaged velocity (m s^{-1}) in the x or y direction, respectively.

To assess the flooding extent in each of our modeling simulations, we produced polygons of the inundated floodplain area and tabulated the percent of the floodplain that was inundated. Additionally, we tabulated the number and area of hydrologic islands (non-inundated areas surrounded by water) in the domain.

We also tabulated the average flooding depth, velocity magnitude, and specific discharge magnitude in the river channel, entire floodplain, and floodplain channels.

This was accomplished using a polygon mask of the river channel, entire floodplain extent, and the floodplain channel masks used to generate the initial conditions (section 3.2.1). Averages and standard deviations were computed as the mean and standard deviations for a half-Gaussian distribution for all cells within the extent of a polygon. A half-Gaussian distribution was chosen because it best fit the data distribution. Trend significance of the results were evaluated using an F-test. Additionally, we computed an average lateral exchange of surface water between the river channel and floodplain and a unit residence time of water in the floodplain. These calculations follow the same procedure outlined by Czuba et al. (2019) and are detailed in the supplementary information. Finally, we mapped our model simulations into an average unit residence time-lateral exchange parameter space (Czuba et al., 2019). This parameter space illustrates how much water is exchanged between the river channel and floodplain and how long it resides in a given location along the floodplain.

4.0 Results

4.1 Spatial variability of flooding is controlled by river-floodplain and down-valley connectivity

Spatial flooding patterns varied among the floodplains with different DVC and RFC. Model simulations with a low DVC have flooded areas close to the main river channel at low flooding discharges (Figure 4). As discharge increased, the flooded area incrementally inundated higher elevation topographic features and extended toward the valley margins (Figure 4a-c). In contrast, simulations with a large DVC allowed floodwaters at lower discharges to reach the valley margins through floodplain channels. As discharge increased for high DVC scenarios, the floodplain segments between floodplain channels became incrementally inundated (Figure 4d-f). Additionally, we found that the spatial distribution of floodwaters was strongly influenced by long-wavelength topography in simulations with a low DVC causing hydrologic islands to form around broad topographic highs (Figure 4a-c). Simulations with a high DVC were weakly influenced by the long-wavelength topography as flow at lower stages was routed though floodplain channels (Figure 4d-f). Simulations with a low RFC caused flooding to inundate the majority of the river banks at low flooding discharges (Figure 4a, b, d), whereas simulations with a high RFC had more variability of wet and dry banks at lower discharges (Figure 4c, e, f).

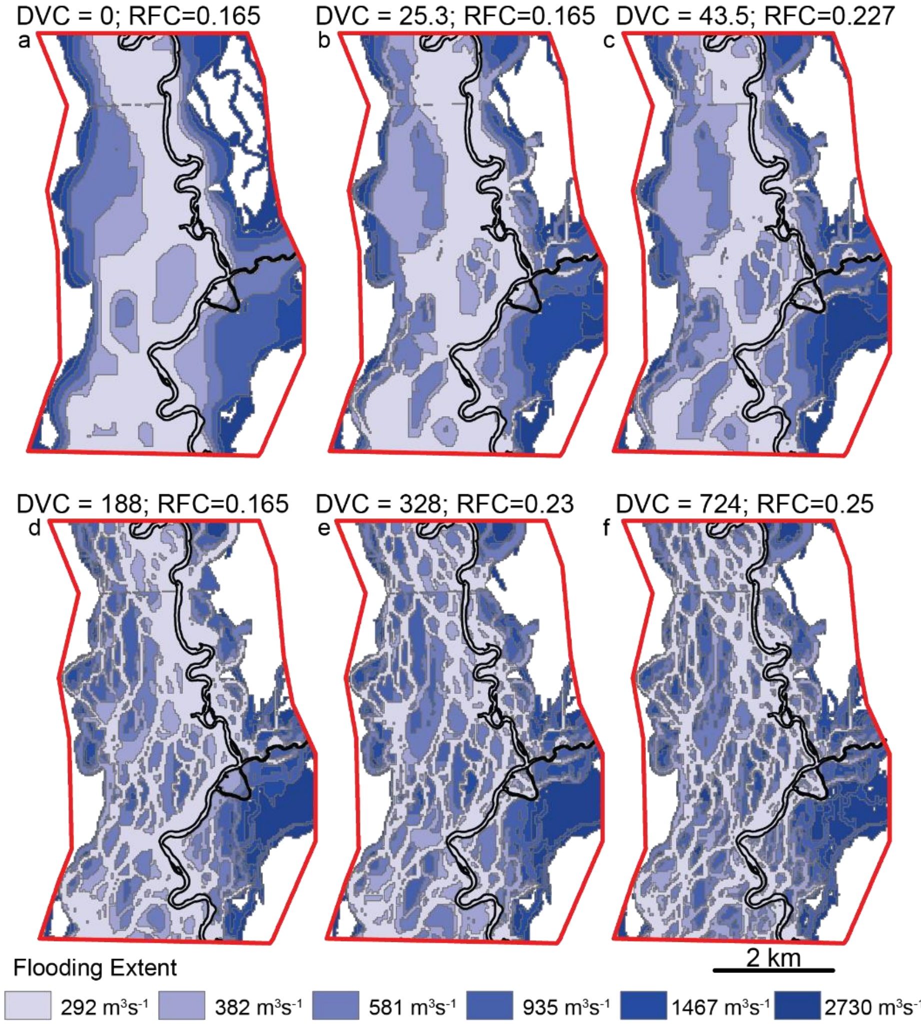

Figure 4. Spatial variability of flooding. a-f) Examples of flooding spatial patterns for six different initial conditions varying DVC and RFC. The shades of blue indicate flooding extent for different discharges, where darker blues show the new areas flooded at progressively higher discharges. The black line delineates the river-channel banks. The example locations are the same reach of river shown in figure 3.

Topographic connectivity also influences the proportion of floodplain that is inundated. Changes in RFC resulted in no statistically significant changes in the proportion of floodplain inundated (Figure 5a). When 80% or more of the floodplain was inundated ($Q=935 m^3s^{-1}$), the influence of DVC was negligible (Figure 5b). However, $Q < 935 m^3s^{-1}$, increasing DVC decreased the percent of floodplain inundated because water is confined within channels (Figure 5b). Analysis of the number of hydrologic islands in the floodplain showed that increasing DVC and RFC increased the number of hydrologic islands (Figure 5c, d). As the number of islands increases, we expect more spatially varied flood pathways as water takes increasingly tortuous paths across the floodplain. As discharge increases for a given DVC and RFC we generally find the number of hydrologic islands increase until a discharge of 581 m^3s^{-1}, beyond which the number of hydrologic islands decreases with increasing discharge (Figure 5c, d).

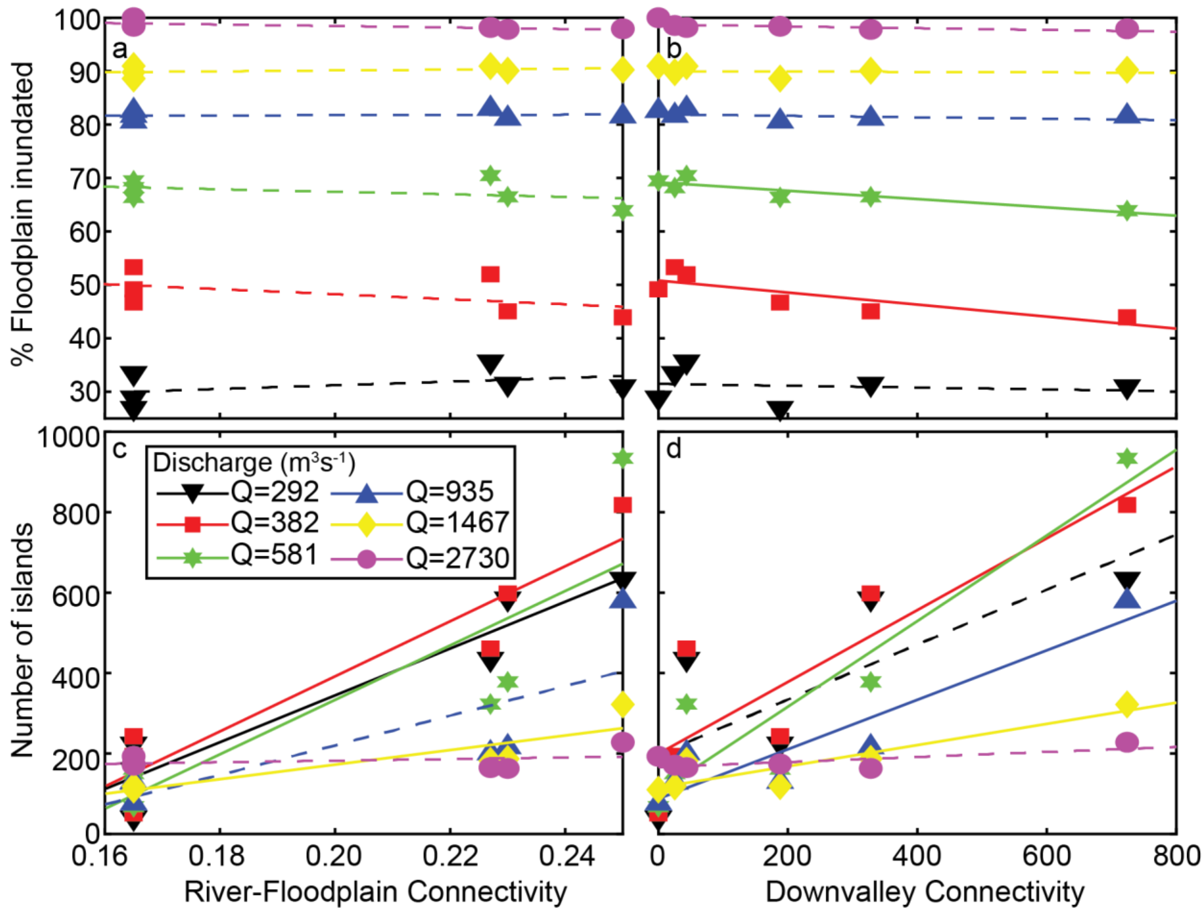

Figure 5. Inundated area and island analysis for entire domain. a, b) Percent of floodplain inundated as a function of varying RFC and DVC. The lines show the best fit for each steady state discharge. c, d) Number of hydrologic islands in the floodplain as a function of RFC and DVC. Solid lines indicate trends with statistical significance ($p<0.05$) and dashed line are not statistically significant.

4.2 Increases in DVC and RFC have the most influence on surface-water flow characteristics at lower flooding discharges

In nearly all cases, changes in DVC and RFC only have statistically significance when the incoming discharge is less than 382 $m^3\ s^{-1}$ (e.g. Figure 6-8). At these low flooding discharges increasing RFC and DVC generally causes the depth (Figure 6a, b) and specific discharge (Figure 6e, f) in the main channel to decrease. The effect on the main channel velocity is unclear (Figure 6c, d). The response across the entire floodplain show that the average velocity and specific discharge increase with increasing connectivity ($p < 0.05$ for Q = 292 and 382 $m^3 s^{-1}$; Figure 7c-f). Flow characteristics within the floodplain channels did not significantly change as a function of DVC or RFC.

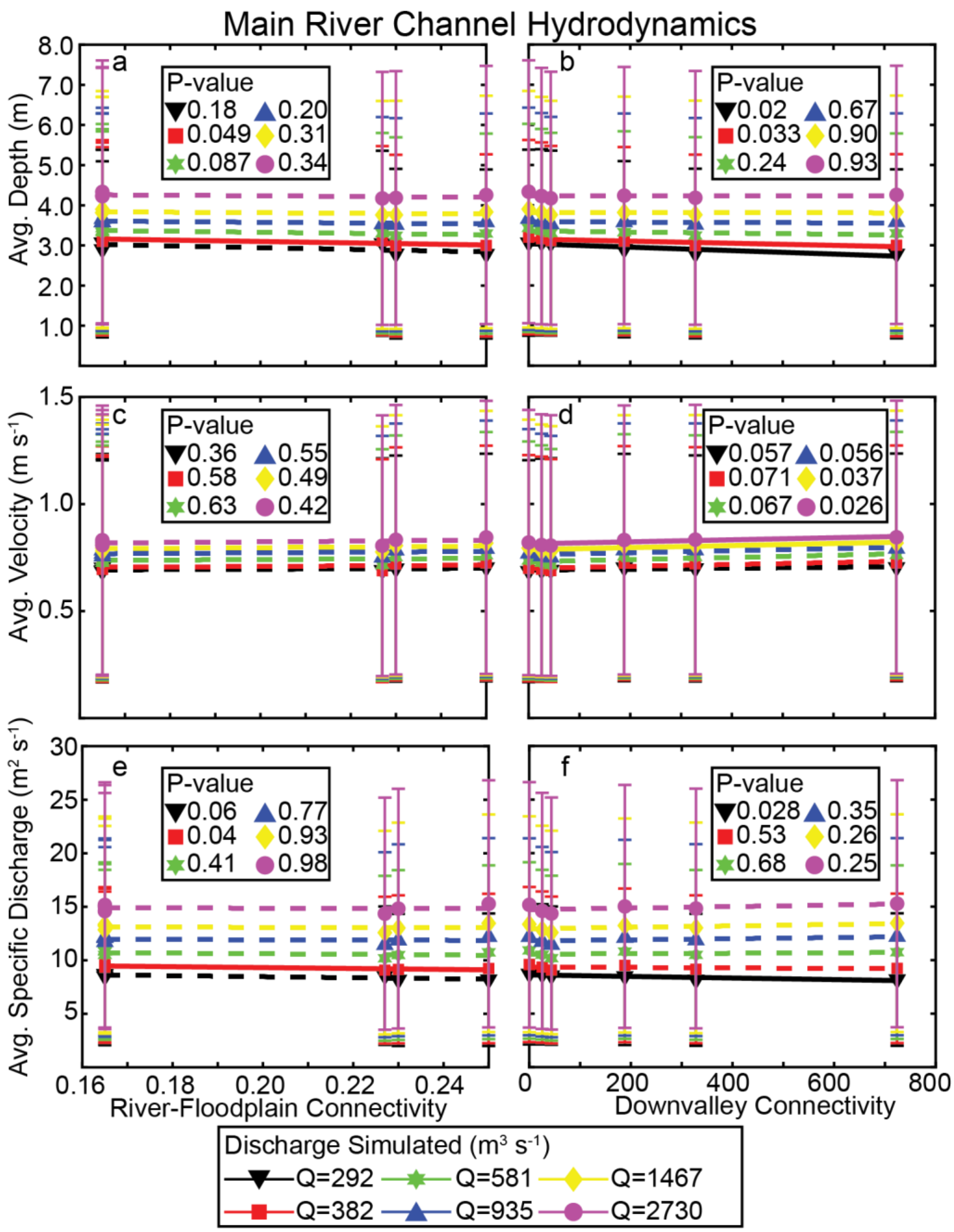

Figure 6. Spatially averaged main river channel flow dynamics throughout the domain. The colored lines are the best fit for each steady state discharge simulated and error bars show one standard deviation in the data. Solid lines indicate trends with statistical significance (P<0.05) and dashed line are not statistically significant.

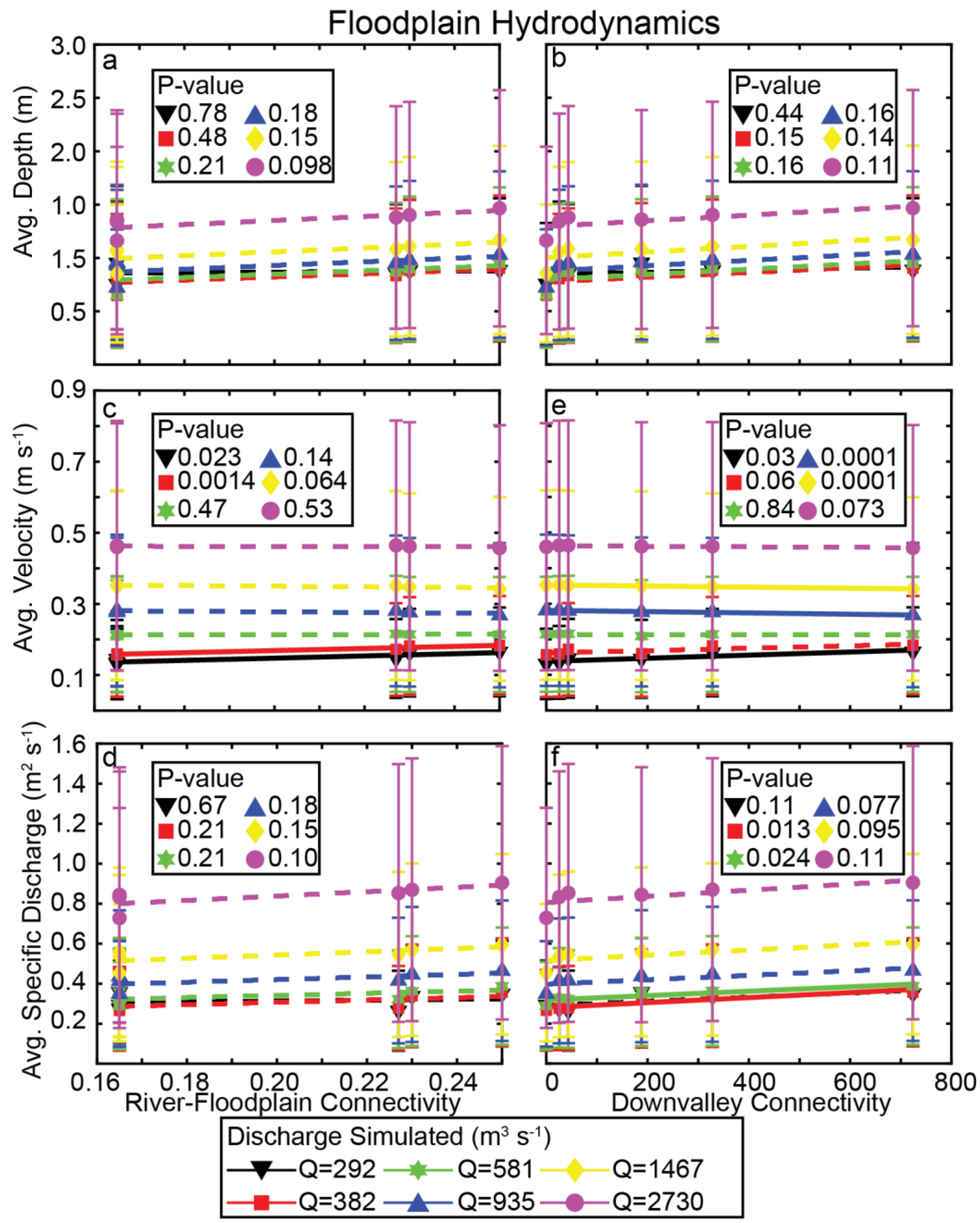

Figure 7. Spatially averaged flow dynamics in the floodplain. The colored lines are the best fit for each steady state discharge simulated and error bars show one standard deviation in the data. Solid lines indicate trends with statistical significance ($p<0.05$) and dashed line are not statistically significant.

4.3 Controls on the lateral exchange and residence time of surface water

Lateral exchange of surface waters between the river and floodplain is predominantly controlled by river stage. We find no significant trends between lateral exchange and RFC or DVC (Figure 8a, b). At low flooding discharges, residence time in the floodplain decreased as RFC increased (Figure 8c). For higher discharges, residence time increased slightly as DVC increased (Figure 8d).

At low flooding discharges, we found that a low DVC maximized the lateral exchange and average residence time for water in the floodplain (Figure 8e). At higher discharges, larger RFC maximized the lateral exchange-unit residence relationship (Figure 8e). In general, our results suggest that floodplains with moderate DVC and high RFC will promote the highest lateral exchange-unit residence time under most discharges.

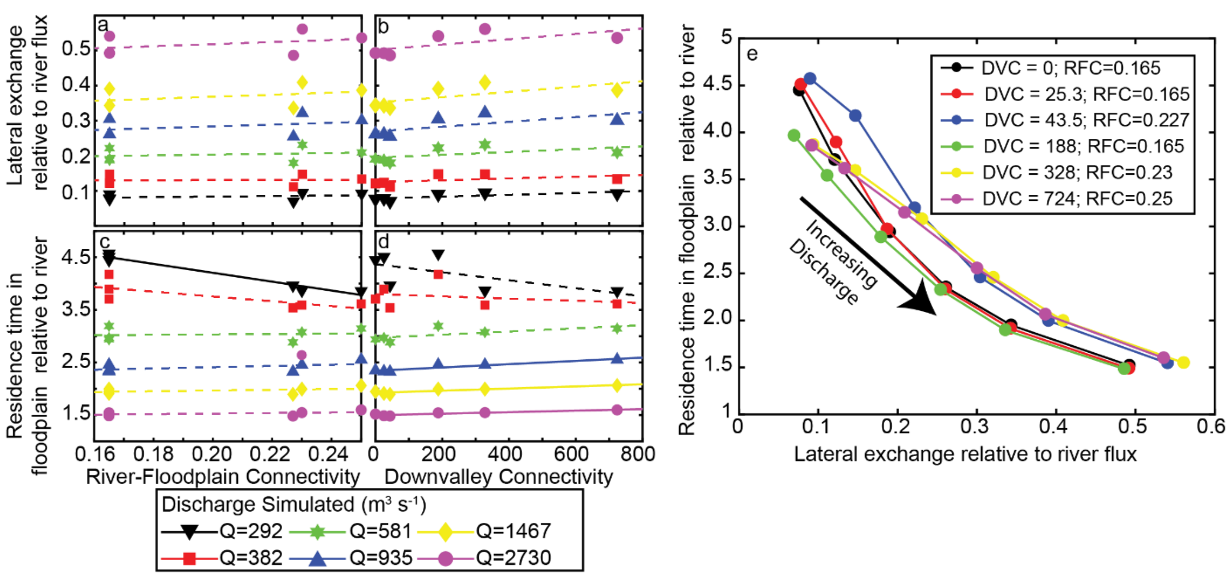

Figure 8. Unitless lateral exchange and unitless residence time. Colored lines in a-d show best fits for each simulated discharge, solid lines indicate trend is statically significant ($P<0.05$) and dashed lines indicate non-statically significant trend. a, b) Average lateral exchange between the river channel and floodplain normalized by the average flux through the river channel as a function of RFC and DVC. c, d) Average residence time-per-unit length of floodplain normalized by the average residence time-per-unit length in the river as a function of RFC and DVC. Simulations varying RFC showed a statistically significant trend for a discharge of 292 $m^3 s^{-1}$ ($P=0.00048$). Variations in DVC showed statistically significant trends at discharges of 935 $m^3 s^{-1}$, 1467 $m^3 s^{-1}$, and 2730 $m^3 s^{-1}$ ($P=0.006$, $P=0.013$, $P=0.01$, respectively). e) Exchange-residence time parameters space. Colored lines indicate results for different initial RFC and DVC values.

4.4 Increases in DVC and RFC influence floodwave propagation

Our steady state simulations suggest that increasing DVC and RFC should drive floodwave attenuation by increasing flow path lengths (Figure 4) and increasing volume of water flowing in the floodplain (Figure 8f). To see how increasing DVC and RFC affects floodwave attenuation, we ran an additional six models for the smoothed floodplain (Figure 4a) and the natural floodplain (Figure 4f). Our simulations show that floodplain channels do attenuate floodwaves and their influence is accentuated at lower discharges (Figure 9a). We find that from our simulations with floodwaves of a peak discharge 292 m^3s^{-1}, 581 m^3s^{-1}, and 1467 m^3s^{-1} the floodplain channels resulted in a 3.5%, 1.8%, and, 0.16% percent increase in floodwave attenuation, respectively (Figure 9a). Additionally, we find that the majority of floodwave attenuation occurs at the initial portion of the rising limb and the final portion of the falling floodwave limb Figure (9b-d), further suggesting floodplain channels have the strongest influence on flood hydrodynamics at lower flooding discharges.

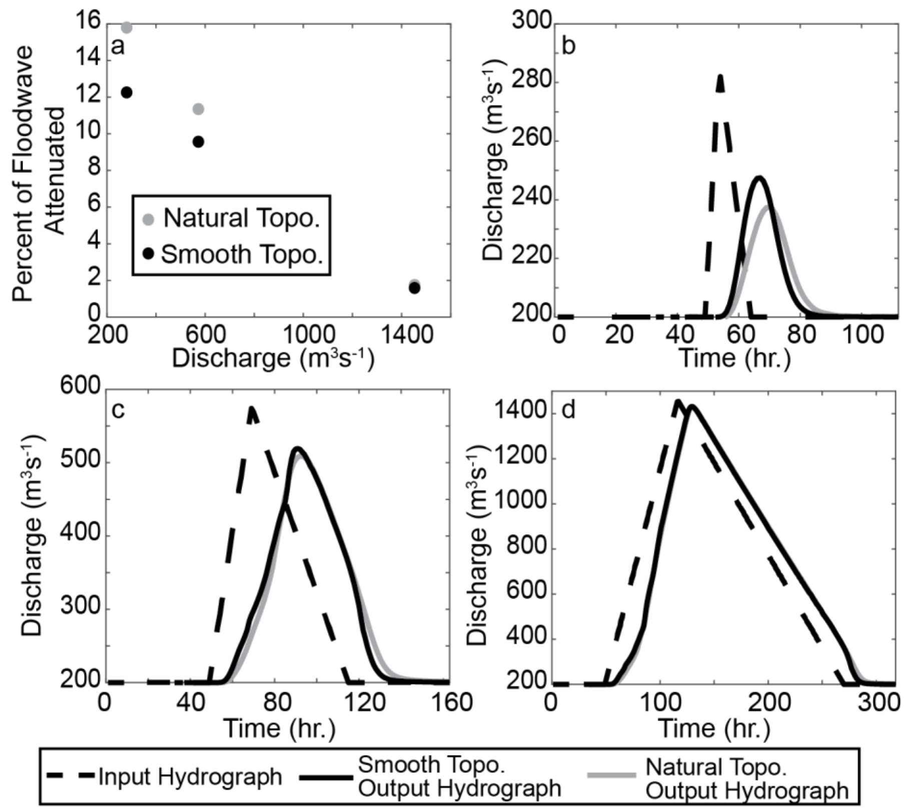

Figure 9. Floodwave dynamics. a) Plot showing percentage of peak discharge attenuated for the existing topography (grey) and the smoothed topography (black). b-d) Plots showing how the resulting hydrographs were reshaped from the initial input hydrograph (black dashed line) to the downstream hydrograph for the smooth (black solid line) and natural (grey solid line) topography.

5.0 Discussion

5.1 Floodplain channels alter how floodplains become inundated

Floodplain channel presence is an important control on flooding processes and floodplain hydrodynamics. For instance, consider the classical model for river flooding based on the notion of bankfull discharge (Leopold et al., 1964; Williams, 1978), where after a river stage threshold is met water spills over the banks and spreads out across the floodplain. Our model simulations with no floodplain channels and floodplain channels with a low DVC behave similarly to the classical model (Figure 4a-c). In these simulations, water spilled over the banks and incrementally increased the wetted width until reaching the valley walls, creating hydrologic islands around only long-wavelength topography. In contrast, simulations with a high DVC and at the lowest discharges, water extended out to the floodplain margins (Figure 4d-f) and created many hydrologic islands across the floodplain surface (Figure 5d). As discharge increases, the water level in the floodplain channels rises inundating the floodplain segments between floodplain channels (Figure 4d-f). Hence, when DVC is high, floodplains are inundated from water rising in the floodplain channels, rather than from the widening of the wetted flood pool. Similar flooding patterns have been observed on the Congaree River in South Carolina (Kupfer et al., 2015) and the Ogeechee River in Georgia (Benke et al., 2000).

Our results show that floodplain inundation pattern is more sensitive to DVC than to RFC (compare Figure 4a-c to d-f). This suggests that floodplains with a high DVC do not conform to the classical model of overbank topping and floodplain inundation during low discharge flooding events. Hence, classical models are insufficient to characterize the complex transitions from river channel to overbank flow, which are important to consider given that low discharge flooding events occur frequently in these systems (Czuba et al., 2019). Accounting for floods occurring before all river banks are overtopped is important as it will create increased variability in wet-dry transitions along the river banks and in the floodplain (Figure 4d-f). The increased variability should promote the development ecological and bio-geochemical hotspots (Frei et al., 2012) in floodplains with a high DVC, thus affecting floodplain functioning.

5.2 Increases in RFC promote increased floodplain functioning by increasing exchange and residence time

We applied the methodological framework outlined by Czuba et al. (2019) for quantifying lateral exchange and residence-time parameter space of surface water. This parameter space allows us to examine the quantity and duration of water on the floodplain in our model runs (Figure 8e). It is worth noting that our computed residence time is measured as a time-per-unit length in the floodplain and in the river, rather than a total time along the entire pathway.

In this parameter space (Figure 8e) we can explore how DVC and RFC influence floodplain functioning. The upper right corner of the parameter space indicates when the most water enters the floodplain and resides there the longest. This portion of parameter space should maximize the ability of a floodplain to attenuate floodwaves (Lininger and Latrubesse, 2016), recharge aquifers (Morin et al., 2009; Sophocleous, 2002), and store sediment, solutes, and nutrients (Junk et al., 1989; Mitsch & Gosselink, 2000; Tockner & Stanford, 2002; Walling, 1999). Our results suggest that higher RFC pushes floodplain functioning towards this space. Surprisingly, DVC has virtually no impact on residence time or lateral exchange (Figure 8e). This suggests to us that the processes that drive RFC are also important for floodplain functioning even if they do not strongly affect inundation patterns.

As we have shown, floodplain channels have an influence on the functioning of floodplains especially in their role to increase RFC. Because of this they should be considered in floodplain restoration projects. Restoration projects often rely on the removal of artificial levees to enhance lateral connectivity of rivers and floodplains (Opperman et al., 2009; Tockner & Stanford, 2002). Floodplains are often engineered after the classical meandering river model (Nanson & Croke, 1992), which presents floodplains as relatively flat, featureless accumulations of sediment. However, our models show that topographic connectivity of the floodplain influences flooding processes and may alter floodplain functioning when compared to a relatively featureless floodplain. For example, increasing topographic connectivity increases the volume and residence time of water in the floodplain (Figure 8e), which would enhance solute diffusion (Bryant-Mason et al., 2013; Forshay & Stanley, 2005; Tockner et al., 1999), sediment deposition and retention (Croke et al., 2013; Malard et al., 2002; Tockner et al., 1999), and water infiltration into the subsurface (Morin et al., 2009; Sophocleous, 2002). Floodplain restoration, guided by our results, would benefit by considering how floodplain channels connecting to the main river channel enhance restoration efforts.

5.3 Floodplain channels affect floodwave propagation at low flooding discharge

Floodplain channel connectivity may also have important implications for floodwave dynamics. We already know that topographic lows on floodplains have been shown to aid in floodwave attenuation through water retention and adding topographic roughness. For instance, paleo-meander cutoffs attenuated the peak flood by 30% on the Araguaia River in Brazil (Lininger & Latrubesse, 2016). Moreover, paleo-meander cutoffs can be linked together by secondary channels to form an integrated floodplain-channel network (David et al., 2017). Our result that floodwave propagation is affected by floodplain channels at low discharges is consistent with these ideas and the recent modeling results from Czuba et al., (2019). They showed that as the floodplain became more inundated the surface-water flow paths were less influenced by floodplain channels, which explains why floodplain channels are less effective at attenuating floodwaves during large flooding events.

While our unsteady modeling results suggest that floodplain channels increase floodwave attenuation, we do not simulate some important processes that may further complicate this relationship. For instance, simulations with a high DVC and RFC produce more wet-dry transitions, which could result in increased aquifer recharge that would further attenuate a translating floodwave. Additionally, floodplains with a high DVC and RFC may be able to drain more water, leaving less trapped in topographic lows than a floodplain rich in geomorphic features that are not well connected. Hence, further modeling and field work is necessary to fully assess how floodplain geomorphic connectivity and floodplain channels affect floodwave dynamics.

5.4 Floodplain topography is a critical control on flooding processes at low discharge, frequent flooding

Our modeling results provide insight into understanding the relative roles of a fluctuating hydrograph and the topographic connectivity on setting flood hydrodynamics. The influence of floodplain topography is most significant at the lowest flooding discharges simulated in this study. We only simulated discharges that cause flooding, and when considering the full range of flows, the low flooding discharges simulated here are in the 50-75th percentile of all flows (Czuba et al., 2019). This is not entirely surprising since at high discharges most of the low-relief floodplain topography we investigate here is fully inundated and at the lowest discharges, water remains in the main channel, and floodplain channels are inactive (Czuba et al., 2019). Still, increased RFC creates more lateral exchange even at higher discharges (Figure 8).

Our results suggest that these low-discharge flooding events could be an important part of floodplain functioning. At our study site, low-level floods have a RI of 19 days (Czuba et al., 2019) compared to RIs of once a year (or less frequent) for larger events. Because of their frequency these low-level floods may be important components that drive hyporheic exchange and biogeochemical processing in the floodplain. Both of these processes are sensitive to the kind of smaller-scale topography we investigated here (Frei et al., 2012).

The well-connected topographic configuration of the floodplain surface opens a window for flooding processes to initiate that does not occur in threshold systems that only put water on the floodplain above some bankfull discharge. It remains an open and interesting question exactly how the dynamics of hyporheic exchange and nutrient processing are affected by highly connected river-floodplain systems that repeatedly flood at below bankfull stages.

6.0 Conclusion

In this study, we investigated how the connectivity of floodplain topographic lows influence flooding processes. Results suggest that floodplain topography influences flooding most at low flooding discharges because at high discharge those topographic features are fully inundated and no longer significantly steer flow. With minimal connectivity of topographic lows, floodplain inundation incrementally extends to the valley margins as discharge increases. Whereas at high connectivity, inundation extends to the valley margin at low flooding discharges and creates many hydrologic islands. As discharge increases the hydrologic islands are incrementally inundated. At the lowest discharges simulated here, highly connected floodplain topography, both down-valley and lateral with the river channel, decreases average specific discharge in the main channel because flow is lost to the floodplain. Subsequently, the specific discharge on the floodplain increases as connectivity increases. Additionally at low flooding discharges, high down-valley connectivity decreases residence time of surface waters, whereas at high discharges increased lateral connectivity of the river to floodplain increases lateral exchange. Our results suggest that topographic connectivity between the floodplain and the main channel has an important effect on flooding processes at low flooding discharges by driving surface water exchange and increasing residence time on the floodplain.

7.0 Acknowledgements & Data Availability

SRD would like to acknowledge the Geological Society of America grant number 11550-17 for supporting of this work. DAE would like to thank the donors of the American Chemical Society Petroleum Research Fund for supporting this work and the Indiana University Grand Challenges Preparing for Environmental Change for partial support. JAC was partially supported by Virginia Agricultural Experiment Station and USDA Hatch program (1017457). A portion of ASW's time was supported by National Science Foundation (NSF) awards EAR 1652293 and EAR 1331906, Department of Energy award DE-SC0019377, and the Burnell and Barbara Fischer Faculty Fellowship at Indiana University.

Land cover, USGS stream flow, 2008 HWMs, aerial imagery, and lidar data is available from Homer et al. (2015), USGS (2018), Morlock et al. (2008) and Indiana Geospatial Data Portal (imagery and lidar; https://gis.iu.edu/), respectively. 2018 WSEs, bathymetric data, and polygon masks of active floodplain extent, floodplain channels, and river channel will be made publically available in Indiana University Scholar Works, an open access, repository.

References

Benke, A. C., Chaubey, I., Ward, G. M., & Dunn, E. L. (2000). Flood Pulse Dynamics of an Unregulated River Floodplain in the Southeastern U.s. Coastal Plain. *Ecology*, *81*(10), 2730–2741. https://doi.org/10.1890/0012-9658(2000)081[2730:FPDOAU]2.0.CO;2

Boulton, A. J. (2007). Hyporheic rehabilitation in rivers: restoring vertical connectivity. *Freshwater Biology*, *52*(4), 632–650. https://doi.org/10.1111/j.1365-2427.2006.01710.x

Bracken, L. J., & Croke, J. (2007). The concept of hydrological connectivity and its contribution to understanding runoff-dominated geomorphic systems. *Hydrological Processes*, *21*(13), 1749–1763. https://doi.org/10.1002/hyp.6313

BryantMason, A., Xu, Y. J., & Altabet, M. A. (2013). Limited capacity of river corridor wetlands to remove nitrate: A case study on the Atchafalaya River Basin during the 2011 Mississippi River Flooding. *Water Resources Research*, *49*(1), 283–290. https://doi.org/10.1029/2012WR012185

Costanza, R., d'Arge, R., de Groot, R., Farber, S., Grasso, M., Hannon, B., et al. (1997). The value of the world's ecosystem services and natural capital. *Nature*, *387*(6630), 253–260. https://doi.org/10.1038/387253a0

Covino, T. (2017). Hydrologic connectivity as a framework for understanding biogeochemical flux through watersheds and along fluvial networks. *Geomorphology*, *277*, 133–144. https://doi.org/10.1016/j.geomorph.2016.09.030

Croke, J., Fryirs, K., & Thompson, C. (2013). Channel-floodplain connectivity during an extreme flood event: implications for sediment erosion, deposition, and delivery: CHANNEL-FLOODPLAIN CONNECTIVITY. *Earth Surface Processes and Landforms*, n/a-n/a. https://doi.org/10.1002/esp.3430

Czuba, J. A., David, S. R., Edmonds, D. A., & Ward, A. S. (2019). Dynamics of Surface-Water Connectivity in a Low-Gradient Meandering River Floodplain. *Water Resources Research*, *55*(3), 1849–1870. https://doi.org/10.1029/2018WR023527

David, S. R., Edmonds, D. A., & Letsinger, S. L. (2017). Controls on the occurrence and prevalence of floodplain channels in meandering rivers: Controls on Floodplain Channels in Meandering Rivers. *Earth Surface Processes and Landforms*, *42*(3), 460–472. https://doi.org/10.1002/esp.4002

David, S.R., Czuba, J. A., & Edmonds, D. A. (2019). Channelization of meandering river floodplains by headcutting. *Geology*, *47*(1), 15–18. https://doi.org/10.1130/G45529.1

Di Baldassarre, G., Viglione, A., Carr, G., Kuil, L., Salinas, J. L., & Blöschl, G. (2013). Socio-hydrology: conceptualising human-flood interactions. *Hydrology and Earth System Sciences*, *17*(8), 3295–3303. https://doi.org/10.5194/hess-17-3295-2013

Fagan, S. D., & Nanson, G. C. (2004). The morphology and formation of floodplain-surface channels, Cooper Creek, Australia. *Geomorphology*, *60*(1–2), 107–126. https://doi.org/10.1016/j.geomorph.2003.07.009

Forshay, K. J., & Stanley, E. H. (2005). Rapid Nitrate Loss and Denitrification in a Temperate River Floodplain. *Biogeochemistry*, *75*(1), 43–64. https://doi.org/10.1007/s10533-004-6016-4

Frei, S., Knorr, K. H., Peiffer, S., & Fleckenstein, J. H. (2012). Surface micro-topography causes hot spots of biogeochemical activity in wetland systems: A virtual modeling experiment. *Journal of Geophysical Research: Biogeosciences*, *117*(G4). https://doi.org/10.1029/2012JG002012@10.1002/(ISSN)2169-8961.SYNTHESIS1

Homer, C., Dewitz, J., Yang, L., Jin, S., Danielson, P., Coulston, J., et al. (2015). Completion of the 2011 National Land Cover Database for the Conterminous United States – Representing a Decade of Land Cover Change Information. *PHOTOGRAMMETRIC ENGINEERING*, 11.

Junk, W. J., Bayley, P. B., & Sparks, R. E. (1989). The flood pulse concept in river-floodplain systems. *Canadian Special Publication of Fisheries and Aquatic Sciences*, *106*(1), 110–127.

Kupfer, J. A., Meitzen, K. M., & Gao, P. (2015). Flooding and Surface Connectivity of *Taxodium-Nyssa* Stands in a Southern Floodplain Forest Ecosystem: CONNECTIVITY OF TAXODIUM-NYSSA STANDS. *River Research and Applications*, *31*(10), 1299–1310. https://doi.org/10.1002/rra.2828

Leopold, L. B., Wolman, M. G., & Miller, J. P. (1964). *Fluvial Processes in Geomorphology*. San Francisco, California: W.H. Freeman.

Lininger, K. B., & Latrubesse, E. M. (2016). Flooding hydrology and peak discharge attenuation along the middle Araguaia River in central Brazil. *CATENA*, *143*, 90–101. https://doi.org/10.1016/j.catena.2016.03.043

Malard, F., Tockner, K., Dole-Olivier, M.-J., & Ward, J. V. (2002). A landscape perspective of surface-subsurface hydrological exchanges in river corridors. *Freshwater Biology*, *47*(4), 621–640. https://doi.org/10.1046/j.1365-2427.2002.00906.x

Mertes, L. A. K., Dunne, T., & Martinelli, L. A. (1996). Channel-floodplain geomorphology along the Solimões-Amazon River, Brazil. *Geological Society of America Bulletin*, 19.

Mitsch, W. J., & Gosselink, J. G. (2000). The value of wetlands: importance of scale and landscape setting. *Ecological Economics*, *35*(1), 25–33. https://doi.org/10.1016/S0921-8009(00)00165-8

Morin, E., Grodek, T., Dahan, O., Benito, G., Kulls, C., Jacoby, Y., et al. (2009). Flood routing and alluvial aquifer recharge along the ephemeral arid Kuiseb River, Namibia. *Journal of Hydrology*, *368*(1–4), 262–275. https://doi.org/10.1016/j.jhydrol.2009.02.015

Morlock, S. E., Menke, C. D., Arvin, D. V., & Kim, M. H. (2008). *Flood of June 7-9, 2008, in central and southern Indiana*. US Geological Survey.

Nanson, G. C., & Croke, J. C. (1992). A genetic classification of floodplains. *Geomorphology*, *4*(6), 459–486. https://doi.org/10.1016/0169-555X(92)90039-Q

Opperman, J. J., Galloway, G. E., Fargione, J., Mount, J. F., Richter, B. D., & Secchi, S. (2009). Sustainable Floodplains Through Large-Scale Reconnection to Rivers. *Science*, *326*(5959), 1487–1488. https://doi.org/10.1126/science.1178256

Poeppl, R. E., Keiler, M., elverfeldt, K. V., Zweimueller, I., & Glade, T. (2012). The influence of riparian vegetation cover on diffuse lateral sediment connectivity and biogeomorphic processes in a medium-sized agricultural catchment, austria. *Geografiska Annaler: Series A, Physical Geography*, *94*(4), 511–529. https://doi.org/10.1111/j.1468-0459.2012.00476.x

Rak, G., Kozelj, D., & Steinman, F. (2016). The impact of floodplain land use on flood wave propagation. *Natural Hazards*, *83*(1), 425–443. https://doi.org/10.1007/s11069-016-2322-0

Robinson, B. (2013). USGS Scientific Investigations Report 2013–5168 - Recent (circa 1998 to 2011) Channel-Migration Rates of Selected Streams in Indiana. Retrieved from https://pubs.usgs.gov/sir/2013/5168/

Roley, S. S., Tank, J. L., & Williams, M. A. (2012). Hydrologic connectivity increases denitrification in the hyporheic zone and restored floodplains of an agricultural stream: DENITRIFICATION IN STREAM ECOTONES. *Journal of Geophysical Research: Biogeosciences*, *117*(G3), n/a-n/a. https://doi.org/10.1029/2012JG001950

Rowland, J. C., Stacey, M. T., & Dietrich, W. E. (2009). Turbulent characteristics of a shallow wall-bounded plane jet: experimental implications for river mouth hydrodynamics. *Journal of Fluid Mechanics*, *627*, 423–449. https://doi.org/10.1017/S0022112009006107

Rudorff, C. M., Melack, J. M., & Bates, P. D. (2014). Flooding dynamics on the lower Amazon floodplain: 1. Hydraulic controls on water elevation, inundation extent, and river-floodplain discharge: HYDRAULIC CONTROLS OF FLOODING ON THE LOWER AMAZON. *Water Resources Research*, *50*(1), 619–634. https://doi.org/10.1002/2013WR014091

Sophocleous, M. (2002). Interactions between groundwater and surface water: the state of the science. *Hydrogeology Journal*, *10*(1), 52–67. https://doi.org/10.1007/s10040-001-0170-8

Stanford, J. A., & Ward, J. V. (1993). An Ecosystem Perspective of Alluvial Rivers: Connectivity and the Hyporheic Corridor. *Journal of the North American Benthological Society*, *12*(1), 48–60. https://doi.org/10.2307/1467685

Thayer, J. B., & Ashmore, P. (2016). Floodplain morphology, sedimentology, and development processes of a partially alluvial channel. *Geomorphology*, *269*, 160–174. https://doi.org/10.1016/j.geomorph.2016.06.040

Tockner, K., & Stanford, J. A. (2002). Riverine flood plains: present state and future trends. *Environmental Conservation*, *29*(3), 308–330. https://doi.org/10.1017/S037689290200022X

Tockner, K., Pennetzdorfer, D., Reiner, N., Schiemer, F., & Ward, J. V. (1999). Hydrological connectivity, and the exchange of organic matter and nutrients in a dynamic river–floodplain system (Danube, Austria). *Freshwater Biology*, *41*(3), 521–535. https://doi.org/10.1046/j.1365-2427.1999.00399.x

Trigg, M. A., Bates, P. D., Wilson, M. D., Schumann, G., & Baugh, C. (2012). Floodplain channel morphology and networks of the middle Amazon River: AMAZON FLOODPLAIN CHANNEL MORPHOLOGY AND NETWORKS. *Water Resources*

U.S. Geological Survey (USGS) (2018). *USGS 03365500 East Fork White River at Seymour, IN*. Reston, VA: U.S. Geological Survey. (last accessed 01 Jan. 2018)

Wainwright, J., Turnbull, L., Ibrahim, T. G., Lexartza-Artza, I., Thornton, S. F., & Brazier, R. E. (2011). Linking environmental régimes, space and time: Interpretations of structural and functional connectivity. *Geomorphology*, *126*(3–4), 387–404. https://doi.org/10.1016/j.geomorph.2010.07.027

Walling, D. E. (1999). Linking land use, erosion and sediment yields in river basins. In J. Garnier & J.-M. Mouchel (Eds.), *Man and River Systems* (pp. 223–240). Dordrecht: Springer Netherlands. https://doi.org/10.1007/978-94-017-2163-9_24

Ward, J. V., & Stanford, J. A. (1995). Ecological connectivity in alluvial river ecosystems and its disruption by flow regulation. *Regulated Rivers: Research & Management*, *11*(1), 105–119. https://doi.org/10.1002/rrr.3450110109

Williams, G. P. (1978). Bank-full discharge of rivers. *Water Resources Research*, *14*(6), 1141–1154. https://doi.org/10.1029/WR014i006p01141

Wohl, E., Brierley, G., Cadol, D., Coulthard, T. J., Covino, T., Fryirs, K. A., et al. (2019). Connectivity as an emergent property of geomorphic systems: Geomorphic connectivity. *Earth Surface Processes and Landforms*, *44*(1), 4–26. https://doi.org/10.1002/esp.4434

Water Resources Research

Supporting Information for

The Influence of Floodplain Channel Connectivity on Flood Hydrodynamics

Scott R. David[1,2], Jonathan A. Czuba[3], Douglas A. Edmonds[2], and Adam S. Ward[4]

[1]Department of Geosciences, University of Massachusetts, Amherst, Massachusetts, USA

[2]Department of Earth and Atmospheric Sciences, Indiana University, Bloomington, Indiana, USA

[3]Department of Biological Systems Engineering and The Global Change Center, Virginia Tech, Blacksburg, Virginia, USA

[4]School of Public and Environmental Affairs, Indiana University, Bloomington, Indiana, USA

Contents of this file

Introduction

This supporting information file contains an extended description of the methods that are unique to this study and those that partially overlap with Czuba et al. (2019)

Text S1: 1.0 Extended Methods

1.1.0 Model Development

We developed a 2-D unsteady surface-water hydrodynamic model for the East Fork White River and its adjacent floodplain in HEC-RAS version 5.0.3 using the Saint Venant equations. The computational mesh contained a total of 187,955 cells and used a combination of structured and unstructured meshes. The structured computational mesh has square cells, each 900 m^2. Breaklines were enforced along major roadways (cell spacing of ~3m), river banks, middle of the river (cell spacing of ~12m), and across the low head dam (cell spacing of ~1.5m; Figure S1) producing the unstructured portion of the mesh. A spatially varied Manning's roughness was applied to the mesh, based on 30 m resolution land cover data (Homer et al., 2015),and the coefficients were chosen based on model calibration discussed in section 1.2. The topography data used in the model was a 1.5m digital elevation model (DEM) derived from light detection and ranging (lidar) data, bathymetric data, and theoretical topography for connectivity scenarios constructed by modifying the empirical elevation datasets. The topographic and bathymetric data collection and manipulation is described in section 1.1.1. Boundary conditions were set at three locations on the model grid: the upstream model extent of the East Fork White River, the upstream model extent of Sand Creek, and the downstream model extent of the East Fork White River (Figure S1). Our choice in boundary conditions is discussed in section 1.1.2.

1.1.1 Topography and Bathymetry Data

Topographic data used in the model consisted of a combination of empirical and theoretical topographic datasets. The empirical data used were constructed from a 1.5m DEM derived from aerial lidar flown on March 23, 2011 (http://www.indianamap.org). The lidar sensor could not measure topography through surface water, hence data points with water on the day of data acquisition were removed and replaced with a flat or sloping plane, a process called hydro-flattening. But the geometry of the main channel is important for the flooding processes we seek to understand here. We surveyed the river channel using a single-beam acoustic profiler measuring water depth and spatial location. The portion of the reach we surveyed is shown with a yellow line in figure 1. Additionally, we measured water-surface profiles with a real-time kinematic geographic position system (RTK-GPS) along the river during the day of surveying. To construct the bed-elevation surface we subtracted the depth data from the measured water-surface elevation data. Bed elevation data were processed into a DEM by taking the average depth along 30 m (approximately half the average river width) segments of the river centerline. The average depth along the segment was then assigned to a cross-section along that river segment. A triangulated irregular network was generated from the cross-sections, averaging all cross-channel variability while maintaining down-valley pool and riffle sequences. River reaches without bathymetric data were lowered by 1.5m to match the overall slope of our measured bathymetric data.

In addition to the actual topography, we also generated five synthetic floodplains based on the East Fork White River floodplain with various degrees of floodplain channel and river-floodplain connectivity. The synthetic floodplain surfaces were generated by extracting the extent of the East Fork White River active floodplain at the 89-year flood of record. We then removed all floodplain channels from the floodplains surface by applying a Gaussian filter (Eqn. 1) as:

$$G(x,y) = \frac{1}{\sqrt{2\pi\sigma^2}} e^{-\frac{x^2+y^2}{2\sigma^2}} \qquad \text{Eqn. 1}$$

where, x and y are spatial distances (meters) and σ is the standard deviation of the Gaussian distribution. The calculation used σ = 6 m and iterated over the active floodplain 20 times, creating a preliminary smoothed floodplain. The presence of the floodplain channels caused artificially low inter-channel areas during the spatial averaging. To overcome this, we removed and interpolated all portions of the active floodplain ~0.1m lower than the preliminary smoothed surface. This eliminated most floodplain channels and the river channel. Additionally, we removed all major road features in the active floodplain domain to avoid any artificial increases in floodplain elevation. We applied the same Gaussian filter as before to the active floodplain with the floodplain channels, river channel, and roads removed, thus producing a smoothed version of the East Fork White River floodplain that maintains long wavelength topography. The river channel, roads, and terraces were then added back into the smoothed floodplain topography creating a floodplain with a similar long wavelength topography and floodplain extent, but without floodplain channels (Figure 2).

We used the smoothed floodplain (Figure 3a) and existing floodplain (Figure 3f) to generate four additional floodplains with different topographic connectivity between the floodplain channels and the river channel. We envision different floodplain-channel network connectivity as being related to the degree of channelization. The present floodplain surface is channelized with a highly integrated floodplain-channel network, and the smooth floodplain surface is the least channelized. We create intermediately channelized floodplains by selectively preserving the deepest parts of the channel network. This creates a floodplain with channel segments that are not connected. To do this we detrend the natural floodplain with the smoothed floodplain, thereby creating a normalized DEM where negative values represent elevations lower than the smoothed floodplain. We then use two floodplain channel masks with threshold values of -0.23 m and -0.84 m and remove all channel cells above the thresholds. This creates two surfaces that isolate and preserve only the lowest-lying floodplain channel cells (threshold of -0.84 m) and both low-lying and mid-elevation floodplain channels (threshold of -0.23 m). The two channel masks were used to extract floodplain channels from the existing topography and add them back to the smoothed floodplain topography. The threshold of -0.84 m created a floodplain with weakly connected floodplain channels (Figure 4c), and the threshold of -0.23 m created a floodplain with better connected floodplain channels (Figure 4e).

Additionally, we constructed two synthetic floodplains with the same floodplain-channel connectivity as described above, but we also changed the strength of connections between the floodplain channel and the main river (Figure 3b, d). To accomplish this, all floodplain channels were removed from the two floodplain channel masks within 60 m (approximately two times the average levee width) of the river channel. This effectively removes all natural breaks in the levees and banks created by channels or crevasses. We created one additional floodplain channel mask to delineate the floodplain channels on the existing floodplain using a threshold of -0.15 m. The mask was used for data analysis and quantifying initial conditions.

To quantitatively describe our six different initial conditions, we developed a metric to describe the connectivity within the floodplain-channel networks (hereafter down-valley connectivity, DVC). DVC was calculated as:

$$DVC = \frac{F_{CA}}{F_{TA}} \times F_I \qquad \text{Eqn. 2}$$

where, F_{CA} is the floodplain channel surface area (m^2), F_{TA} is the total floodplain area (m^2), and F_I is the number of floodplain segments surrounded by floodplain channels (an approximation to assess the number of floodplain channel connections). F_{CA} was calculated with the floodplain channel masks used to extract floodplain channels (described above). F_{TA} was measured based on the wetted extent of the 89-year flood (peak of record) from Czuba et al., (2019). Hence, larger DVC values indicate a greater number of well-connected floodplain channels across the floodplain.

Similarly, we describe the connectivity between the floodplain and main channel as river-floodplain connectivity (RFC). RFC was computed as the coefficient of variation (standard deviation/mean) of the bank height within 30 m (approximately average levee width) of the river channel (Figure 3g). Larger RFC values represent river banks with higher topographic variability, hence an enhanced connection of the river channel to floodplain channels.

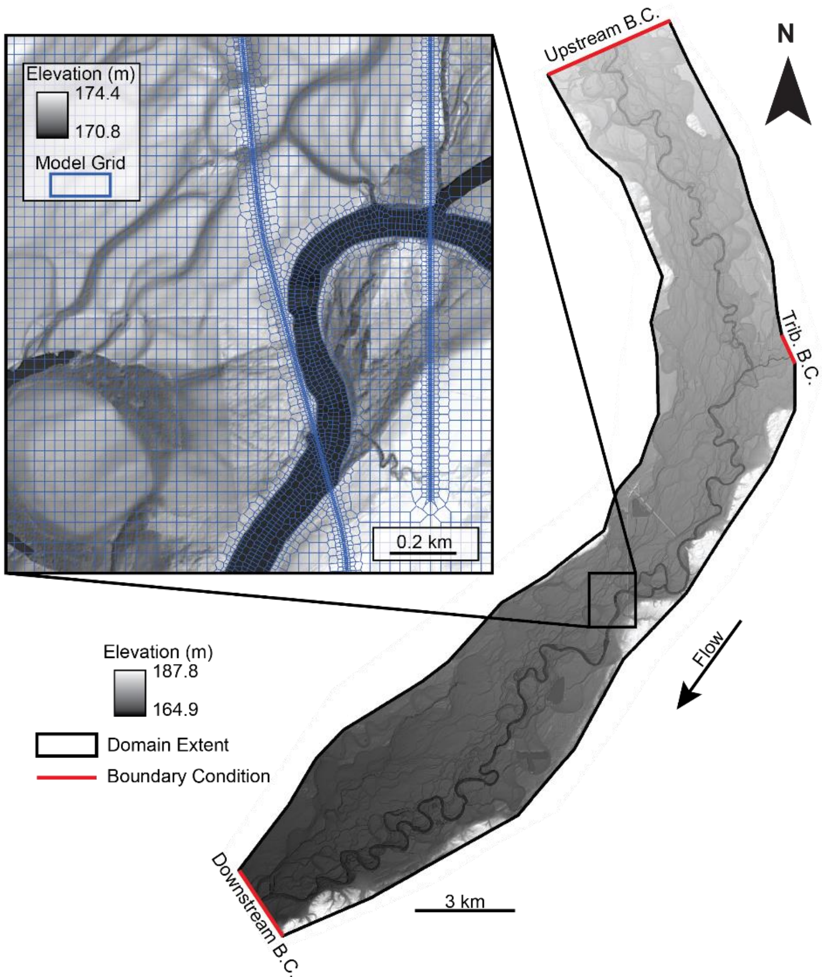

Figure S1*. Model setup along the East Fork White River. The inset shows an example of the computational grid used in the study. Note the floodplain contains a structured grid, while the river and roads have unstructured grids. Locations of the boundary conditions are shown with red lines.*

1.2 Boundary Conditions

The upstream boundary conditions were specified along the East Fork White River and Sand Creek (Figure S1) as a quasi-steady state discharge entering the domain. The quasi-steady state simulations held the discharge entering the domain constant until equilibrium was achieved throughout the entire domain before increasing the discharge (Figure 3h). Discharge entering the domain at the upstream boundaries was chosen based on modeling work by Czuba et al. (2019), which simulated a variety of discharges (7-day to 89-yr. recurrence interval; RI) on the same reach of the East Fork White River. For our modeling experiments, we used six different discharges ranging from 292 m^3s^{-1} to 2,730 m^3s^{-1} which spanned a range of floodplain inundation extents (Figure 3h). Discharges were specified as 90% of the flow entering the domain from the East Fork White River and 10% entering along Sand Creek, based on comparing relative drainage areas. The downstream boundary was specified along the downstream extent of the East Fork White River and its floodplain was set as normal depth (Figure S1). The computation of normal depth required a friction slope (energy grade line slope) which was set to 0.001 along the boundary. The six simulated discharges and six initial conditions created a total of 36 simulations exploring steady state discharges. Additionally, we ran six simulations for unsteady discharges using the smoothed and existing topography. For the unsteady simulations, we specified no discharge entering the domain along the Sand Creek boundary condition and specified a hydrograph at the upstream boundary for the East Fork White River. The input hydrographs were triangular shaped that had peak discharges of 292 m^3s^{-1}, 581 m^3s^{-1}, and 1467 m^3s^{-1}, respectively. The rising limb of the floodwave increased at a rate of 18.7 m^3s^{-1} per hour and the falling limb decreased at a rate of 8.2 m^3s^{-1} per hour. The rates for rising and falling floodwave limb is based on a 10-year average of all rising and falling limbs of floodwaves at the gage in Seymour, IN (USGS, 2018; Figure 9).

1.3 Calibration and Validation

We calibrated the model to the elevation-discharge rating curve developed for the USGS gage located near Seymour, IN (USGS, 2018; Figure 1). Model calibration was conducted by varying Manning's roughness coefficients for the open water (river channel) and agricultural land cover classes (Homer et al., 2015). Final roughness coefficients for the open water and agricultural land cover classes were 0.022 and 0.025 (Table S1), respectively. The final calibrated roughness coefficients in our study differs from those in Czuba et al. (2019) due to the use of the Saint Venant equations rather than the diffusive wave equations. Comparing our model simulations to the elevation-discharge rating curve, we obtained a root mean squared error (RMSE) of 0.16 m and a mean average error (MAE) of 0.15 m. The error we obtained from our model simulations was within the error of the USGS field data used to compute the elevation-discharge rating curve (RMSE= 0.26 m, MAE = 0.18 m; Figure S2a).

Land cover class	Default *n*	Final *n*
Agricultural Vegetation	0.04	0.025
Open Water	0.035	0.022
Forest & Woodland	0.12	0.12
Undifferentiated Barren Land	0.04	0.04
Developed, Open Space	0.04	0.04
Developed, Low Intensity	0.08	0.08
Developed, Medium Intensity	0.1	0.1
Developed, High Intensity	0.15	0.15

Table S1. Land cover classes and their associated Manning's Roughness coefficients (*n*). The table shows the default Manning's Roughness coefficients (Brunner, 2016) based on land cover classes and our final coefficients after calibration.

Model validation was accomplished using surveyed high-water marks collected by the USGS in 2008 (Morlock et al., 2008), water-surface elevations collected during flooding in February, 2018, and aerial imagery of flooding collected in April, 2011 (locations shown in Figure 1). The 2008 high-water marks were measured using mud, drift, debris, and seed lines on trees, fences, buildings, and utility poles (Morlock et al., 2008) as a proxy for maximum water-surface elevation. The measurements corresponded to the peak of record on June 8, 2018 with a discharge of 2,730 m^3s^{-1}. The 2018 water-surface elevations were measured on February 26, 2018 using RTK-GPS and corresponded to a flow of ~890 m^3s^{-1} at the USGS gage in Seymour, IN. Comparing our model simulation of the existing topography to the measured high-water marks gave a RMSE of 0.51m and a MAE of 0.46m (Figure S3b). A comparison between our model simulation and direct measurements of water-surface elevations collected in 2018 was more accurate with a RMSE of 0.17 m and a MAE of 0.12 m (Figure S3b).

The aerial photo of flooding (Figure S2c) was taken on April 7, 2011 at ~12:30 pm corresponded to a discharge of ~657 m^3s^{-1} and a water-surface elevation of 127.7 m at the USGS gage in Seymour, IN. Comparing our model simulation with a discharge of ~657 m^3s^{-1} and a water-surface elevation of 172.9 m (at the location of the river gage) to the aerial imagery, the simulation slightly over-predicts the extent of inundation, but still captures the majority of land-water transitions (Figure S2d) in high detail.

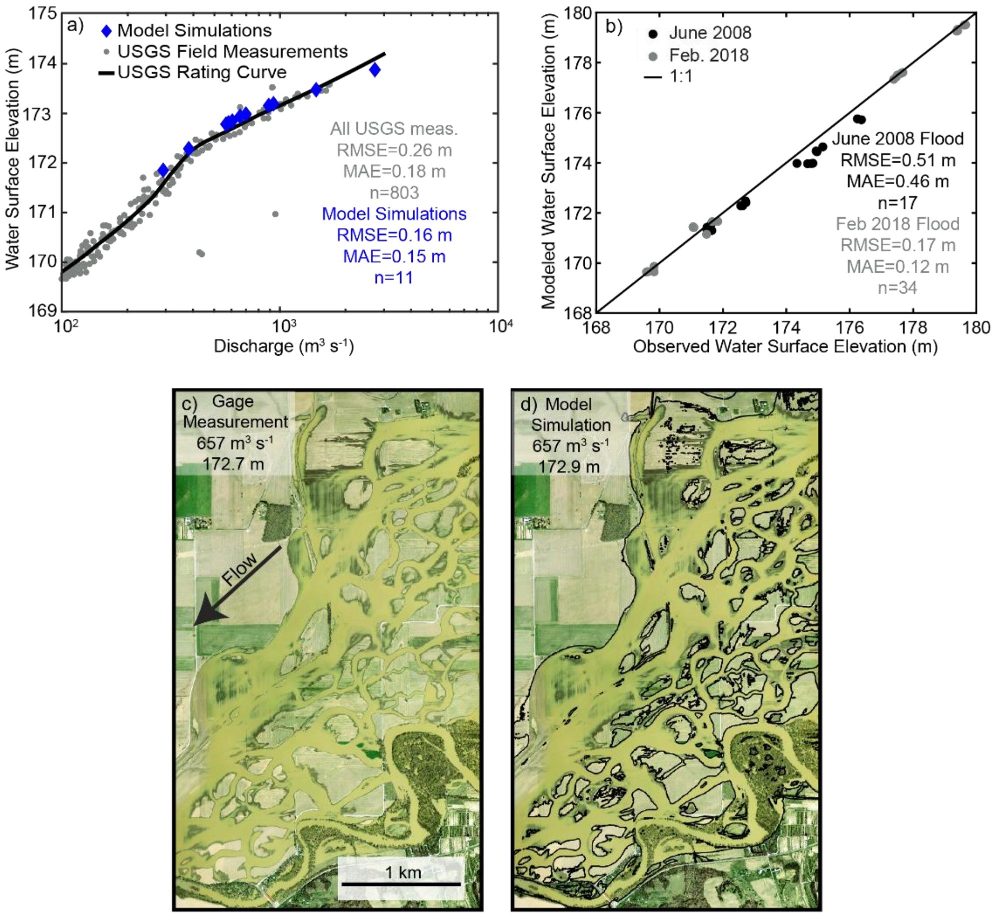

Figure S2. *Model calibration and validation data. a) Model calibration to the elevation-discharge rating curve, gage location is shown in Figure 1. b) Simulated vs. measured water surface elevations for high water marks measured from the peak record flood in June 2008 and water surface elevations from flooding on Feb. 26, 2018. c) Aerial photography of flooding on April 7, 2011. d) Model simulation showing transition of water to land as black lines corresponding to the same discharge when the image was taken.*

3.3 Data Analysis

Initial model outputs from our 36 modeling experiments included water depth, depth averaged velocity magnitude, and 2-D (x and y directed) depth averaged velocity for each cell. We gridded the results at a 15-m resolution for all analysis. From the initial model outputs, we computed the magnitude of specific discharge (q, Eqn. 3) and a 2-D specific discharge ($q_{x,y}$; Eqn. 4) for each grid cell in all model simulations as:

$$q = \bar{v} * h \qquad \text{Eqn. 3}$$

and

$$q_{x,y} = \overline{v_{x,y}} * h \qquad \text{Eqn. 4}$$

where, $\bar{v}$ is the depth-averaged magnitude of velocity (m s^{-1}), h is water depth (m), and $\overline{v_{x,y}}$ is the 2-D depth-averaged velocity in the x or y direction, respectively (m s^{-1}).

To assess the flooding extent in each of our modeling simulations, we produced water masks from our depth data. Water masks were constructed by converting the gridded depth data into polygons and merging the depth polygons into a single polygon representing the wetted extent of the floodplain. The wetted extent polygons were then used to compute the percent of the floodplain that was inundated. Additionally, water masks were used to compute the number and area of hydrologic islands in the domain. Hydrologic islands are defined as dry areas surrounded by water.

We measured the average flooding depth, velocity magnitude, and specific discharge magnitude in the river channel, entire floodplain, and floodplain channels. This was accomplished using a polygon mask of the river channel, entire floodplain extent, and floodplain channel masks used to generate the initial conditions (section 3.2.1). Averages and standard deviations were computed as the mean and standard deviations for a half-Gaussian distribution for all cells within the extent of a polygon. Trend significance of the results were evaluated using a F-test.

We computed an average lateral exchange of surface water between the river channel and floodplain for each steady state model run. Lateral exchange was measured perpendicular to lines situated parallel and positioned 30 m (approximate levee width) from the river banks. The lines were discretized into 90 m long segments and the average q_x and q_y were calculated over each 90m line segment. Between vertices, along the 90 m line segment, we used vector decomposition to solve for the magnitude of specific discharge perpendicular to each line segment (q_p, m s^{-1}), where positive q_p values indicate a flux into the river channel and negative values indicate a flux into the floodplain. The average lateral exchange for each side of this river ($\overline{q_{ex}^{L,R}}$, L is river left and R is river right) is calculated as:

$$\overline{q_{ex}^{L,R}} = \left(\sum_j \left|q_j^{L,R}\right| d_j^{L,R}\right) \frac{1}{D^{L,R}} \qquad \text{Eqn. 5}$$

where, $d_j^{L,R}$ (meters) is the length of individual line segment j and $D^{L,R}$ (meters) is the total distance of all line segments along a given side of the river. The absolute value was taken to account for all flux between the river channel and floodplain. Whereas if the absolute value was not taken, we would compute a net flux between the river and floodplain giving a value of ~0, as flow entering the river and exiting the river would negate each other. The lateral exchange through the left and right side of the river were added together and normalized by the average specific discharge in the river channel ($\overline{q_r}$) to produce normalized unitless river-floodplain exchange (q_{ex}; Eqn. 6).

$$q_{ex} = \frac{\overline{q_{ex}^{L}} + \overline{q_{ex}^{R}}}{\overline{q_r}} \qquad \text{Eqn. 6}$$

To assess the unit residence time of water in the floodplain, we used a defined network of simulated flow paths that were manually traced by Czuba et al. (2019) in the upper portion of our domain. Flow paths were delineated by systematically increasing discharge, and all new flow paths were traced for each increase in flow. In total, there were 23,211 paths mapped with a cumulative distance of ~1,050 km (Figure S3). Average flow velocity (v_i; m s^{-1}) was calculated for each line segment that existed in the wetted extent of each model simulation. A length-averaged velocity ($\overline{v_f}$; m s^{-1}) in the floodplain over all the line segments was computed as:

$$\overline{v_f} = \frac{(\sum v_i l_i)}{L} \quad \text{Eqn. 7}$$

where, l_i is the length of a line segment and L is the length of the total active flow paths. A residence time per unit length of floodplain (t_f; s m^{-1}) was calculated as the inverse of v_f, which describes the time water spends along a certain length scale. Additionally, we calculated a residence time per unit length for the river (t_c; s m^{-1}) by taking the inverse of the average magnitude of velocity in the river channel. We normalized unit residence time (t_r) by the residence time in the river, creating a unitless residence time in the system as:

$$t_r = \frac{t_f}{t_c} \quad \text{Eqn. 8}$$

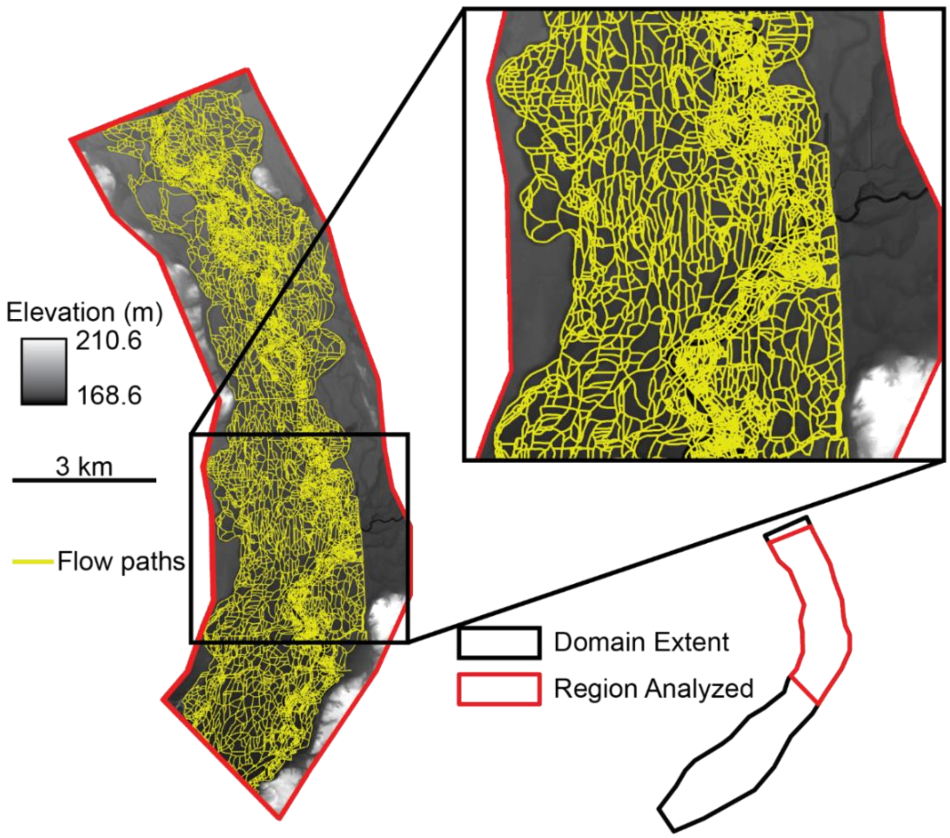

Figure S3. *Flow paths for unit residence time calculation. The yellow lines show the flow paths delineated by Czuba et al. (2019), used to compute the average unit residence time in the floodplain. The portion of the domain for which the analysis was performed is shown in red and the entire model domain is shown in black.*